# Multimodal locally resonant metamaterials for orthotropic structures

**D. Giannini** [1], **M. Schevenels** [2], **E.P.B. Reynders** [1]
[1] KU Leuven, Department of Civil Engineering, Structural Mechanics Section
Kasteelpark Arenberg 40, 3001, Leuven, Belgium
e-mail: **daniele.giannini@kuleuven.be**

[2] KU Leuven, Department of Architecture, Architectural Engineering Research Group
Kasteelpark Arenberg 1, 3001, Leuven, Belgium

## Abstract
Locally resonant metamaterials are used to increase the sound insulation of a host structure, by introducing bandgaps for wave propagation. While most solutions employ periodic layouts with translational resonators, this paper investigates the potential associated with rotational and multimodal resonators. In order to study the associated vibroacoustic phenomena, a comprehensive analytical model based on dynamic effective mass density is first derived. Subsequently, both translational and rotational modes are combined in multimodal resonator layouts. This results in an effective multimodal locally resonant metamaterial, for which accurate and efficient predictions are achieved by combining the proposed analytical model with the modal effective masses of the fixed-based resonator. Finally, it is demonstrated how multimodal metamaterials can suppress the broad coincidence dip in the diffuse transmission loss of orthotropic host plates, and the geometry of two realizable multimodal resonators is optimized to maximize the related broadband sound insulation.

## 1 Introduction

An emerging research field in recent years is related to vibroacoustic metamaterials, for which a growing interest is captured by the possibility of achieving bandgaps for acoustic and elastic wave propagation, i.e. frequency ranges in which no free wave propagation is possible. In particular, recent focus has been on locally resonant metamaterials (LRMs) [1, 2], that allow to obtain resonance-based bandgaps by periodically attaching local resonators to a host structure. The bandgaps are obtained close to the resonance frequencies of the resonators, and they result from the Fano-like interference between incoming waves and out-of-phase re-radiated waves by the local resonators [1]. The main advantage of LRMs is that they allow to target low frequency bandgaps, despite keeping a low mass per unit area.

The presence of bandgaps in a mechanical structure allows for strong vibration attenuation, as well as sound radiation and transmission reduction when acoustically relevant bending waves are targeted. In particular, LRMs can be applied to achieve thin and lightweight acoustic partitions with improved sound transmission loss (TL). For single panels, an interesting focus is on exploiting resonance-based bandgaps to suppress the sharp TL dip around the critical frequency. This case has been extensively studied in [3], where also an analysis on the optimal frequency of the resonators is performed.

Once the desired resonance frequency is chosen, next question is how to design the geometry of a realizable physical LRM resonator that matches the defined requirements. Since a general design methodology is not available, this is typically a trial and error process, based on engineering judgement [4]. In order to obtain an efficient and automatic design process, numerical optimization can be employed [4, 5]. Optimization of resonating structures is gaining significant interest in different domains, such as MEMS [6, 7] and vibroacoustics [5, 8]. Numerical optimization techniques usually require an iterative evaluation of the objective function to be optimized, via a simulation of the system performance. Therefore, the computational cost of

the employed prediction model is one of the crucial points in the design optimization of LRM systems.

The simplest prediction models consider infinite panels with attached single degree of freedom (SDOF) resonators [3, 9], and propose an analytical vibroacoustic description based on the concepts of effective medium and dynamic effective mass density. However, the idealization towards SDOF resonators limits the accuracy and the applicability of analytical models for realisable resonators. Other methods are based on a finite element description of a single unit cell (UC) of the LRM, that is studied by imposing Bloch-Floquet periodicity conditions [10]. This easily allows to compute the TL of LRMs when considering complex resonator geometries [2, 11, 12]. However, despite the development of several model order reduction (MOR) strategies [13], for complex LRMs the analysis can become computationally expensive, due to the high number of involved degrees of freedom in the UC model. Alternatively, hybrid analytical-numerical approaches have been recently developed. In [5], the bandgap width of a LRM plate is maximized by studying only the fixed-base resonator by finite elements and maximizing the modal effective mass of the main mode of interest. In [4], the finite element model of the UC is only used to compute the impedance of the LRM panel, that is then employed to analytically compute the TL.

While most of the recent literature works focus on translational resonators, in this paper the potential of rotational and multimodal resonators is investigated. While translational resonators transfer transversal forces to the host structure, rotational resonators influence wave propagation by transferring bending moments that depend on the specific propagation direction. In order to study the wave propagation and sound transmission phenomena in LRMs with both translational and rotational resonators, we derive a comprehensive analytical description based on the concept of dynamic effective mass density. This opens the way to combine translational and rotational modes in LRMs with complex multimodal resonator layouts, that can help improving sound insulation in a broad frequency range. In this case, efficient predictions of the multimodal LRM can be obtained by combining the analytical model with the extraction of translational and rotational modal effective masses from a simple modal analysis of the fixed-based resonator. As a showcase, we apply periodic multimodal resonators to suppress the broad coincidence TL dip of orthotropic plates. The geometrical layout of two multimodal resonator are numerically optimized through Genetic Algorithms (GAs), in order to maximize broadband sound insulation for diffuse incident sound fields.

The present paper is organized as follows. Section 2 recalls the main vibroacoustic characteristics of orthotropic plates, with focus on the presence of a broadband coincidence dip. In Section 3, the analytical model of orthotropic LRM plates based on dynamic effective mass density is presented, when considering attached SDOF translational and SDOF rotational resonators. Section 4 discusses how multimodal orthotropic LRM plates with complex resonators can be described by combining analytical predictions with modal effective masses extracted for the fixed-base resonator. Two selected multimodal resonator layouts are then optimized for maximum broadband sound insulation. Finally, Section 5 gives conclusions and remarks.

## 2 Vibroacoustics of orthotropic plates

In this Section, we summarize the main vibroacoustic properties of orthotropic plates, namely the directional dependence of bending stiffness and the presence of a broadband coincidence dip for diffuse field sound transmission.

For thin, homogeneous orthotropic plates with thickness $h$, four independent elastic constants are required to characterize the plate bending: the Young's moduli $E_\mathrm{x}$, $E_\mathrm{y}$, the shear stiffness $G_\mathrm{xy}$ and the Poisson's ratio $\nu_\mathrm{xy}$. For harmonic external loads as defined in Figure 1, i.e. a pressure $p(x,y,t) = P\mathrm{e}^{\mathrm{j}(k_\mathrm{x}x+k_\mathrm{y}y+\omega t)}$ and bending moments per unit of area $q_\mathrm{x}(x,y,t) = Q_\mathrm{x}\mathrm{e}^{\mathrm{j}(k_\mathrm{x}x+k_\mathrm{y}y+\omega t)}$ and $q_\mathrm{y}(x,y,t) = Q_\mathrm{y}\mathrm{e}^{\mathrm{j}(k_\mathrm{x}x+k_\mathrm{y}y+\omega t)}$, the equation of motion in terms of the harmonic transverse (bending) displacement $w(x,y,t) = W\mathrm{e}^{\mathrm{j}(k_\mathrm{x}x+k_\mathrm{y}y+\omega t)}$ can be written by considering the equilibrium of an infinitesimal portion of the plate:

$$-\rho h\omega^2 W + \left(D_\mathrm{x}k_\mathrm{x}^4 + 2Hk_\mathrm{x}^2k_\mathrm{y}^2 + D_\mathrm{y}k_\mathrm{y}^4\right)W = -\rho h\omega^2 W + D(\phi)k^4 W = P - \mathrm{j}k_\mathrm{x}Q_\mathrm{x} - \mathrm{j}k_\mathrm{y}Q_\mathrm{y} \qquad (1)$$

where $\rho$ is the mass density of the plate, $D_\mathrm{x} = \frac{E_\mathrm{x}h^3}{12(1-\nu_\mathrm{xy}\nu_\mathrm{yx})}$ and $D_\mathrm{y} = \frac{E_\mathrm{y}h^3}{12(1-\nu_\mathrm{xy}\nu_\mathrm{yx})}$ are the flexural stiffnesses of the plate along the $x$ and $y$ directions, and $H = D_\mathrm{x}\nu_\mathrm{yx} + 2D_\mathrm{xy}$ with $D_\mathrm{xy} = \frac{G_\mathrm{xy}h^3}{12}$, $\nu_\mathrm{xy}E_\mathrm{y} = \nu_\mathrm{yx}E_\mathrm{x}$. $W$, $P$,

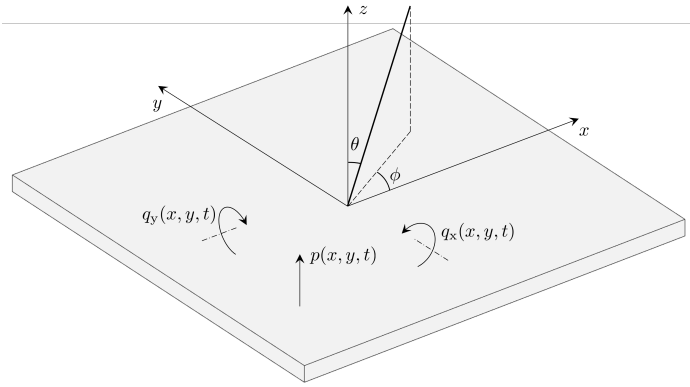


Figure 1: Scheme of the considered orthotropic plate and distributed loads, along with the elevation angle $\theta$ and azimuthal angle $\phi$ for an incident plane wave.

$Q_\mathrm{x}$, $Q_\mathrm{y}$ are the complex-valued amplitudes of plate deflection and the loads, and $k_\mathrm{x} = k\cos\phi$, $k_\mathrm{y} = k\sin\phi$ are the projections of the wavenumber $k$ along the $x$, $y$ directions when referring to a propagation direction defined by the azimuthal angle $\phi$ (cf. Figure 1). In Eq. (1), $D(\phi) = D_\mathrm{x}\cos^4\phi + 2H\cos^2\phi\sin^2\phi + D_\mathrm{y}\sin^4\phi$ can be interpreted as the bending stiffness of the orthotropic plate in the direction $\phi$. When damping is taken into account, complex bending and shear stiffnesses can be introduced through the loss factor $\eta_0$, i.e. $D_\mathrm{x}$, $D_\mathrm{y}$, $H$ can be substituted by $D_\mathrm{x}(1+\mathrm{j}\eta_0)$, $D_\mathrm{y}(1+\mathrm{j}\eta_0)$ and $H(1+\mathrm{j}\eta_0)$.

The dispersion relation along direction $\phi$, i.e. the relation between frequency $\omega$ and wavenumber $k(\omega,\phi)$ for free wave propagation, results directly from Eq. (1) when considering a homogeneous equation of motion:

$$\rho h\omega^2 = D(\phi)k(\omega,\phi)^4 \tag{2}$$

For a plane incident sound wave whose propagation direction is defined by elevation angle $\theta$ and azimuthal angle $\phi$ (cf. Figure 1), a bending wave in the plate is induced with trace wavenumber $k = k_\mathrm{tr} = \frac{\omega}{c}\sin\theta$, whose projections along the $x$ and $y$ directions are $k_\mathrm{x} = \frac{\omega}{c}\sin\theta\cos\phi$ and $k_\mathrm{y} = \frac{\omega}{c}\sin\theta\sin\phi$. The related transmission loss $R$ can be analytically computed as [14]:

$$R = -10\log_{10}\tau(\phi,\theta), \qquad \tau(\phi,\theta) = \left|\frac{z_\mathrm{f}}{z_\mathrm{f}+z_\mathrm{p}}\right|^2 \tag{3}$$

where $\tau(\phi,\theta)$ is the transmission coefficient. The fluid wave impedance $z_\mathrm{f}$ and the plate wave impedance $z_\mathrm{p}$ are given by:

$$z_\mathrm{f} = 2\rho_0 c(1-\sin^2\theta)^{-1/2} \qquad z_\mathrm{p} = -(\mathrm{j}/\omega)(D(\phi)k^4 - \rho h\omega^2) \tag{4}$$

where $\rho_0$ is the density of the surrounding fluid and $c$ is the speed of sound in the fluid.

For a diffuse incident field, the transmission coefficient can be found by integrating the plane wave transmission coefficient $\tau(\phi,\theta)$ over all possible incident angles:

$$\tau_\mathrm{d} = \frac{\int_0^{2\pi}\int_0^{\theta_\mathrm{l}}\tau(\phi,\theta)\sin\theta\cos\theta\mathrm{d}\theta\mathrm{d}\phi}{\int_0^{2\pi}\int_0^{\theta_\mathrm{l}}\sin\theta\cos\theta\mathrm{d}\theta\mathrm{d}\phi} \tag{5}$$

where $\theta_\mathrm{l}$ denotes the upper limit of the elevation angle to account for the non-ideal diffuseness: $\theta_\mathrm{l} = 85°$ is used in the remainder of the paper.

Coincidence is defined as the resonance phenomenon that occurs when the bending wave speed in the plate is equal to the phase speed of the incident sound wave. For an incident sound wave with elevation angle $\theta$, the speed in the direction parallel to the panel will be $c/\sin\theta$. A significant dip in the sound transmission

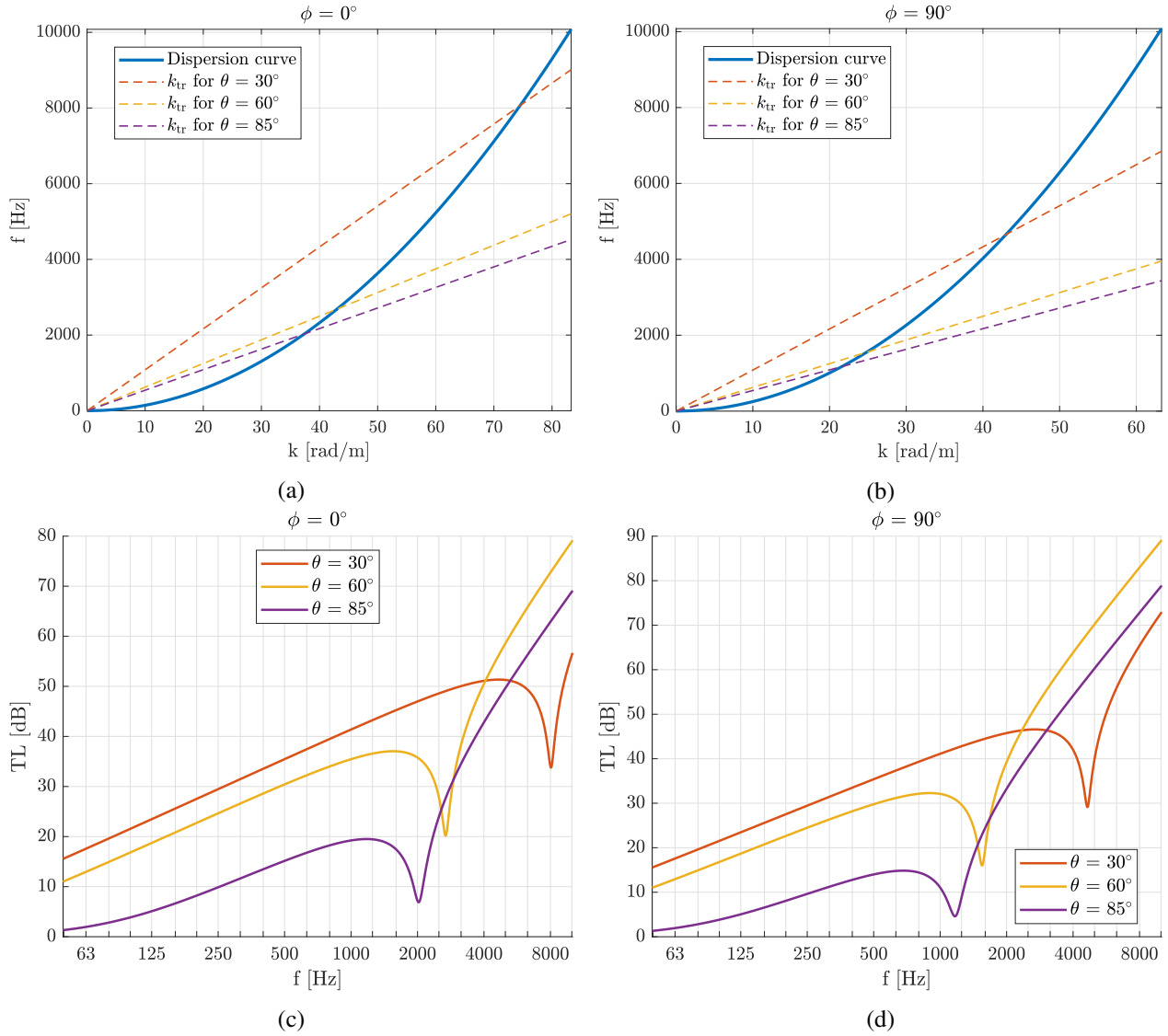


Figure 2: (a,b) Dispersion curves and (c,d) sound transmission loss of the considered orthotropic plate for (a,c) $\phi = 0°$ and (b,d) $\phi = 90°$.

loss appears at the coincidence frequency, that is defined as [15]:

$$f_{\mathrm{co}}(\phi, \theta) = \frac{c^2}{2\pi \sin^2 \theta} \sqrt{\frac{\rho h}{D(\phi)}}. \tag{6}$$

Due to the directional dipendence of the bending stiffness $D(\phi)$, for orthotropic plates the coincidence frequency for an elevation angle $\theta$ depends on the direction of in-plane propagation $\phi$.

In what follows, an orthotropic plate with the following material properties will be considered: $h$ = 15 mm, $\rho$ = 1200 kg/m$^3$, $D_{\mathrm{x}}$ = 1500 Nm, $D_{\mathrm{y}}$ = 4500 Nm, $\eta_0$ = 0.05. Sound transmission in air will be studied, by setting $c$ = 341 m/s and $\rho_0$ = 1.21 kg/m$^3$. Figure 2 shows the related dispersion curves for wave propagation at azimuthal angles $\phi = 0°$ and $\phi = 90°$, along with the TL curves for varying elevation angle $\theta$. The coincidence frequencies of the plate for different elevation angles $\theta$ can be assessed by identifying the intersection of dispersion curves with the incident trace wavenumber curves [14, 16]. Due to the varying coincidence frequency with azimuthal angle $\phi$, a broadening of the coincidence dip in presence of orthotropy appears in the diffuse field TL curve. This is shown in Figure 3, where a comparison with diffuse field TL curves for isotropic plates is provided, when considering isotropic bending stiffnesses equal to $D_x$ and $D_y$.

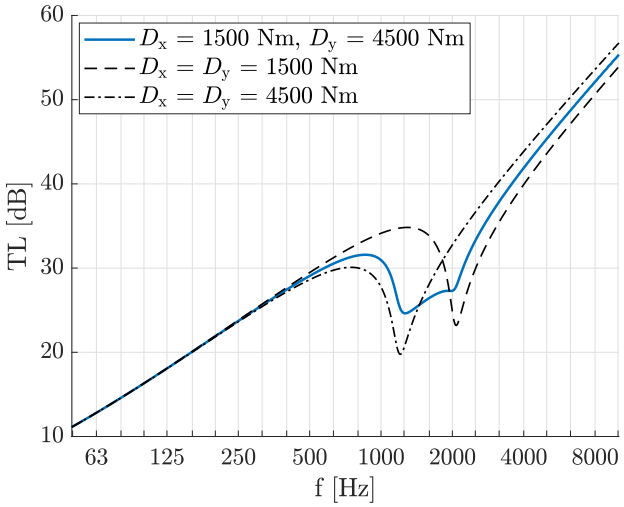


Figure 3: Diffuse field sound Transmission Loss of the considered orthotropic plate.

# 3 Analytical modelling of orthotropic LRM plates with SDOF translational and SDOF rotational resonators

In this Section, the concept of dynamic effective mass density [3, 9] will be introduced to analytically study the vibroacoustic behaviour of orthotropic LRM plates with attached SDOF translational and SDOF rotational resonators.

## 3.1 Orthotropic LRM plates with attached SDOF translational resonators

Let's consider the orthotropic LRM plate whose UC is represented in Figure 4a: the attached resonators have a single vertical translational DOF along $u_z$, mass $m_z$, stiffness $k_z$, and fixed-base resonant frequency $\omega_z = \sqrt{k_z/m_z}$. The size of a single UC is $L_x \times L_y$, and $n = 1/(L_x L_y)$ is the number of resonators per unit area. Resonator damping can be considered through a loss factor $\eta_z$, i.e. by substituting $k_z$ with $k_z(1 + j\eta_z)$.

For a flexural wave with wavelength $\lambda = 2\pi/k$, the resonator displacements and the normal forces transmitted to the host plate are well approximated as continuous, provided that the resonators are attached at a sub-wavelength scale, i.e. the distances among the adjacent elements on the plate surface are significantly smaller than the wavelength [9]. For harmonic motion $w(x, y, t) = We^{j(k_x x + k_y y + \omega t)}$, $u_z = U_z e^{j(k_x x + k_y y + \omega t)}$, the

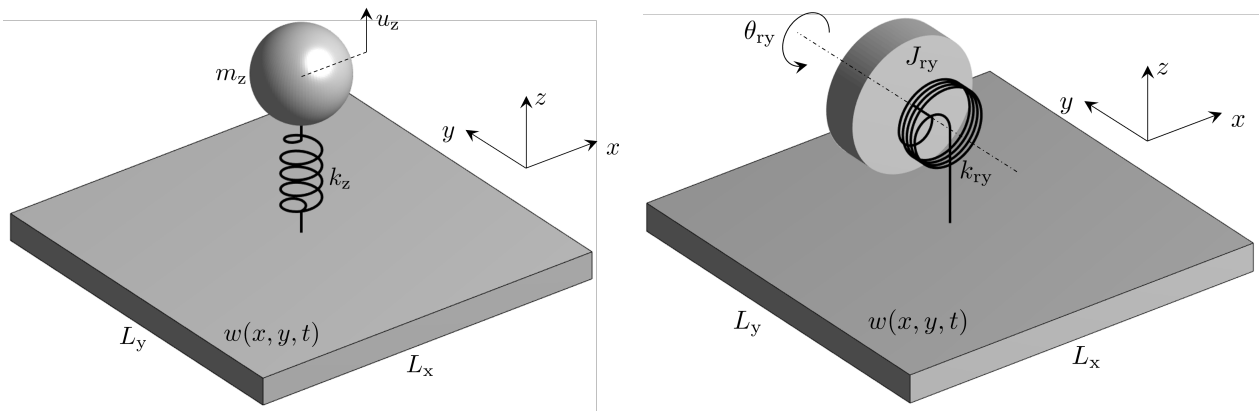


(a) (b)

Figure 4: Scheme of the LRM plate UC when attaching (a) translational and (b) rotational resonators.

equation of motion of the resonator and the continuous transmitted pressure can be written as [3, 9]:

$$\begin{cases} -m_{\mathrm{z}}\omega^2 U_{\mathrm{z}} + k_{\mathrm{z}}\left(U_{\mathrm{z}} - W\right) = 0 \\ P = nk_{\mathrm{z}}\left(U_{\mathrm{z}} - W\right) = nm_{\mathrm{z}}\omega^2 U_{\mathrm{z}} \end{cases} \tag{7}$$

From Eq. (7), the complex amplitudes $P$ of the the pressure transmitted to the plate can be expressed as function of the complex amplitude $W$ of the plate deflection. By substituting such expression into Eq. (1), along with $Q_{\mathrm{x}} = Q_{\mathrm{y}} = 0$, one gets:

$$-\left(\rho h + \frac{nk_{\mathrm{z}}m_{\mathrm{z}}}{k_{\mathrm{z}} - m_{\mathrm{z}}\omega^2}\right)\omega^2 W + D(\phi)k^4 W = 0 \tag{8}$$

The dynamic effective mass density of the LRM can be therefore defined as:

$$\rho_{\mathrm{eff,z}} = \rho + \frac{nk_{\mathrm{z}}m_{\mathrm{z}}}{h\left(k_{\mathrm{z}} - m_{\mathrm{z}}\omega^2\right)} \qquad \rho_{\mathrm{eff,z,und}} = \rho + \frac{nm_{\mathrm{z}}}{h(1 - (\omega/\omega_{\mathrm{z}})^2)} \tag{9}$$

where $\rho_{\mathrm{eff,z,und}}$ is the undamped effective mass density, i.e. for undamped resonators and purely real $k_{\mathrm{z}}$.

From Eq. (9) it results that a negative undamped effective mass is obtained for $\omega_{\mathrm{z}} \leq \omega \leq \omega_{\mathrm{z}}\sqrt{1 + m_{\mathrm{ratio}}}$, where $m_{\mathrm{ratio}} = m_{\mathrm{z}}/m_{\mathrm{UC}}$ is the ratio between the resonator mass $m_{\mathrm{z}}$ and the mass of the host structure $m_{\mathrm{UC}} = \rho h L_{\mathrm{x}} L_{\mathrm{y}}$ within the UC.

The undamped effective mass density found in Eq. (9) can be used in place of the static mass density of the plate $\rho$ in Eq. (2) to study the dispersion relation of the system:

$$k^4 = \frac{\rho_{\mathrm{eff,z,und}}(\omega) h\omega^2}{D(\phi)} \tag{10}$$

From Eq. (10) it can be seen how only imaginary wavenumbers, corresponding to evanescent instead of propagating waves, are found for negative mass densities $\rho_{\mathrm{eff,z,und}}(\omega) \leq 0$. This means that a bandgap with no propagating waves is created for $\omega_{\mathrm{z}} \leq \omega \leq \omega_{\mathrm{z}}\sqrt{1 + m_{\mathrm{ratio}}}$. The effective mass density from Eq. (9) can be also used in place of the static mass density of the plate $\rho$ in Eq. (4) to analytically compute the TL of the system. In particular, a TL peak is expected close to the resonance frequency $\omega_{\mathrm{z}}$ of the resonator, as the magnitude of the effective mass density has a peak close to this frequency.

## 3.2 Orthotropic LRM plates with attached SDOF rotational resonators

The UC of orthotropic LRM plate with attached SDOF rotational resonators, represented in Figure 4b, is now considered: in this case the resonators rotate around the $y$ axis with DOF $\theta_{\mathrm{ry}}$, and are associated with rotational inertia $J_{\mathrm{ry}}$, rotational stiffness $k_{\mathrm{ry}}$, and fixed-base undamped resonant frequency $\omega_{\mathrm{ry}} = \sqrt{k_{\mathrm{ry}}/J_{\mathrm{ry}}}$. Damping can be considered by a loss factor $\eta_{\mathrm{ry}}$, i.e. by substituting $k_{\mathrm{ry}}$ with $k_{\mathrm{ry}}(1 + \mathrm{j}\eta_{\mathrm{ry}})$.

When considering a continuous distribution of rotational resonators, and for harmonic motion $w(x, y, t) = W\mathrm{e}^{\mathrm{j}(k_{\mathrm{x}}x + k_{\mathrm{y}}y + \omega t)}$, $\theta_{\mathrm{ry}} = \Theta_{\mathrm{ry}}\mathrm{e}^{\mathrm{j}(k_{\mathrm{x}}x + k_{\mathrm{y}}y + \omega t)}$, the equation of motion of the resonators and the continuous transmitted bending moment can be written as:

$$\begin{cases} -J_{\mathrm{ry}}\omega^2\Theta_{\mathrm{ry}} + k_{\mathrm{ry}}\left(\Theta_{\mathrm{ry}}(x, y, t) - \mathrm{j}k_{\mathrm{x}}W\right) = 0 \\ Q_{\mathrm{x}} = nk_{\mathrm{ry}}\left(\Theta_{\mathrm{ry}} - \mathrm{j}k_{\mathrm{x}}W\right) = nJ_{\mathrm{ry}}\omega^2\Theta_{\mathrm{ry}} \end{cases} \tag{11}$$

From Eq. (11), the complex amplitude of the transmitted bending moment $Q_{\mathrm{x}}$ can be expressed as function of the complex amplitude $W$ of the plate deflection. By substituting the related expression into Eq. (1), and

considering $P = Q_\mathrm{y} = 0$, the dynamic effective mass density is found as:

$$\rho_{\mathrm{eff,ry}} = \rho + \frac{n k_\mathrm{x}^2 k_\mathrm{ry} J_\mathrm{ry}}{h\left(k_\mathrm{ry} - J_\mathrm{ry}\omega^2\right)}, \qquad \rho_{\mathrm{eff,ry,und}} = \rho + \frac{n k_\mathrm{x}^2 J_\mathrm{ry}}{h(1-(\omega/\omega_\mathrm{ry})^2)} \tag{12}$$

Similarly, the effective mass density for rotational resonators around $x$ can be derived as:

$$\rho_{\mathrm{eff,rx}} = \rho + \frac{n k_\mathrm{y}^2 k_\mathrm{rx} J_\mathrm{rx}}{h\left(k_\mathrm{rx} - J_\mathrm{rx}\omega^2\right)} \qquad \rho_{\mathrm{eff,rx,und}} = \rho + \frac{n k_\mathrm{y}^2 J_\mathrm{rx}}{h(1-(\omega/\omega_\mathrm{rx})^2)} \tag{13}$$

The expressions of $\rho_{\mathrm{eff,ry}}$ and $\rho_{\mathrm{eff,rx}}$ in Eqs. (12) and (13) are similar to the one of $\rho_{\mathrm{eff,z}}$, but with additional scaling factors $k_\mathrm{x}^2$ and $k_\mathrm{y}^2$, that for an incident sound wave defined by $(\phi, \theta)$ become $k_\mathrm{x}^2 = \frac{\omega^2}{c^2}\sin^2\theta\cos^2\phi$ and $k_\mathrm{y}^2 = \frac{\omega^2}{c^2}\sin^2\theta\sin^2\phi$. Some insight into the influence of rotational resonators on the sound transmission of the LRM plate can therefore be discussed:

- The influence of rotational resonators is directional. In particular, the influence of rotational resonators around $y$ is maximum for wave propagation along the $x$-axis and null along the the $y$-axis, as expressed by the factor $\cos^2\phi$. Viceversa, the influence of rotational resonators around $x$ is maximum for propagation along $y$ and null for propagation along $x$, as expressed by the factor $\sin^2\phi$. Also, in general the influence is maximum for (almost) grazing incidence and null for normal incidence, as expressed by the factor $\sin^2\theta$.
- The influence of rotational resonators increases with frequency, as expressed by the factor $\omega^2$.

The effective mass densities in Eqs. (12) and (13) can be used to find the dispersion curves of orthotropic LRM plates with rotational resonators. When considering rotational resonators around the $y$ axis, and in-plane wave propagation defined by an angle $\phi$, the dispersion curve can be found by imposing $\omega$ and solving for $k$. This leads always to the real root:

$$k = \sqrt{\frac{\frac{n\cos^2\phi J_\mathrm{ry}\omega^2}{1-(\omega/\omega_\mathrm{ry})^2} + \sqrt{\frac{n^2\cos^4\phi J_\mathrm{ry}^2\omega^4}{(1-(\omega/\omega_\mathrm{ry})^2)^2} + 4D(\phi)\rho h\omega^2}}{2D(\phi)}} \tag{14}$$

Since wavenumbers are real for all possible frequencies, no bandgap is created. However, a singularity appears at $\omega = \omega_\mathrm{ry}$, where the dispersion curve exhibits a discontinuity.

The TL of orthotropic LRM plates with attached rotational resonators can be predicted by using the analytical formulas in Eqs. (3) and (4), provided that the dynamic effective mass densities in Eqs. (12) and (13) are used in place of the static mass density $\rho$. When the wavenumbers $k_\mathrm{x}$ and $k_\mathrm{y}$ are imposed by the incident wave, the magnitude of the effective mass densities has a peak for frequency approaching the resonance frequencies of the resonators $\omega_\mathrm{ry}$ and $\omega_\mathrm{rx}$, around which a TL peak is expected.

## 3.3 Numerical examples and interpretation

The presented analytical models for orthotropic LRM plates with attached SDOF translational and SDOF rotational resonators are now validated through comparison with the Wave and Finite Element Method (WFEM). Also, a physical interpretation of the results is provided.

The same orthotropic host plate as in Section 2 is considered. In a first case, attached SDOF translational resonators are studied, with the following properties: $\omega_\mathrm{z} = 2\pi f_\mathrm{z}$, $f_\mathrm{z} = \left(f_\mathrm{co}(90°, 85°) + f_\mathrm{c}(0°, 85°)\right)/2 = 1589.5$ Hz, $m_\mathrm{ratio} = 0.2$, $L_\mathrm{x} = L_\mathrm{y} = 0.05$ m. In a second case, periodically attached rotational resonators around the $y$-axis are considered, with the following properties: $\omega_\mathrm{ry} = 2\pi f_\mathrm{ry}$, $f_\mathrm{ry} = 1589.5$ Hz, $J_\mathrm{ry} = J_\mathrm{pua} L_\mathrm{x} L_\mathrm{y}$, $J_\mathrm{pua} = 1.65 \cdot 10^{-2}$ kg, $k_\mathrm{ry} = J_\mathrm{ry}\omega_\mathrm{ry}^2(1 + i\eta_\mathrm{ry})$, where $J_\mathrm{pua}$ is the considered moment of inertia per unit area in the resonator distribution. For both translational and rotational resonators, the resonance frequencies $f_\mathrm{z}$ and $f_\mathrm{ry}$ are therefore tuned in the middle of the coincidence dip of the orthotropic plate.

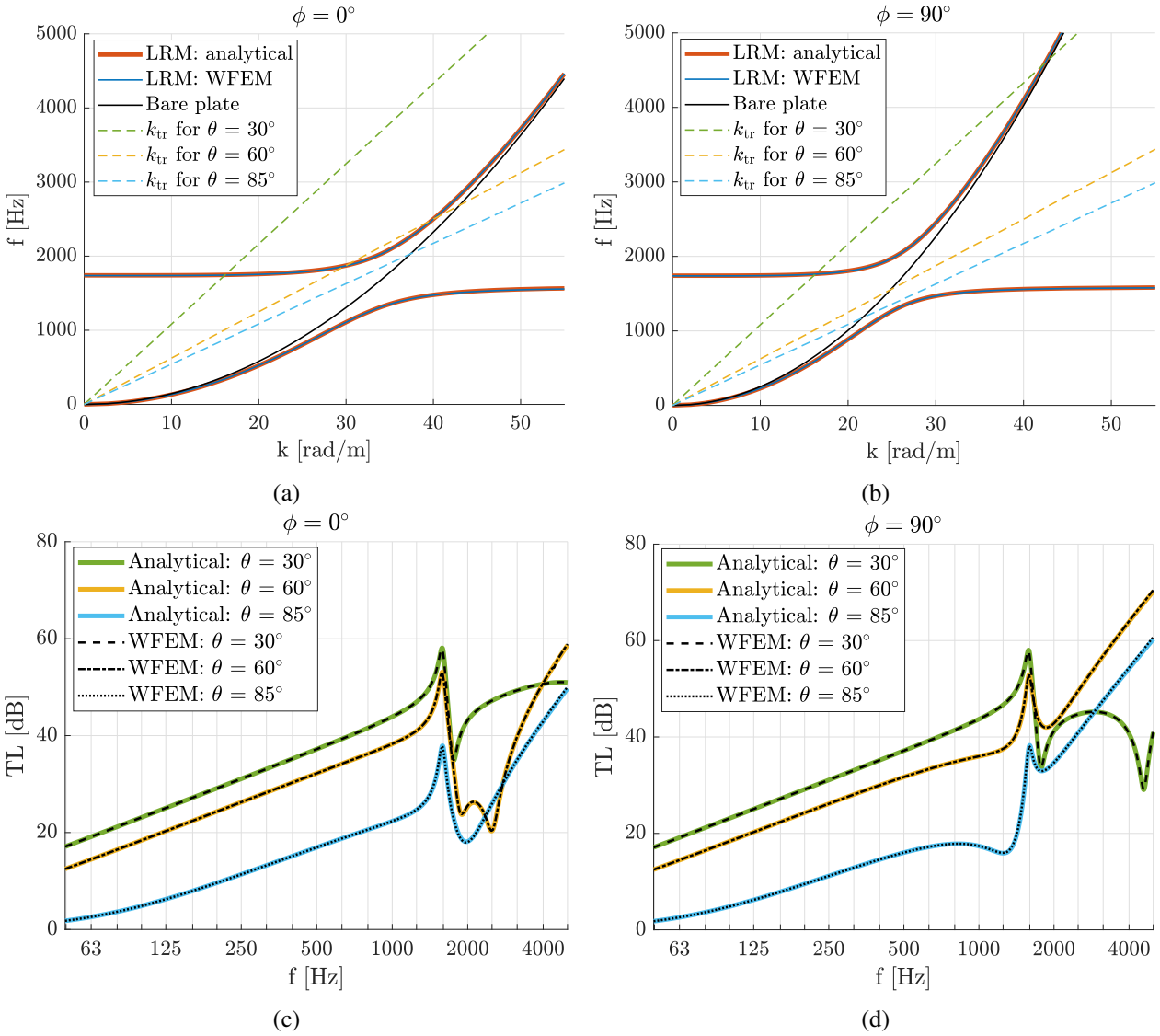


Figure 5: (a,b) Dispersion curves and (c,d) sound transmission loss of the considered orthotropic LRM plate with periodically attached SDOF translational resonators, for (a,c) $\phi = 0°$ and (b,d) $\phi = 90°$.

The analytical models are validate through a comparison with WFEM computations, where one single UC of the periodic LRM plate is modelled, by discretizing the orthotropic plate through linear Kirchhoff plate finite elements, and modelling the resonator as an additional (translational or rotational) DOF attached to the central node of the UC. Bloch-Floquet periodicity conditions are applied, and dispersion curves are obtained by imposing real propagation constants along the directions $x$ and $y$, and solving the resulting linear eigenvalue problem to obtain the squared frequencies $\omega^2$ [10]. The sound TL can be instead computed following the methodology proposed in [17]: the finite element model of the UC is combined with an analytical description of wave propagation in the surrounding fluids, and the interaction with the structure is modelled through a series of equivalent nodal forces. In this way, the response to a convected harmonic pressure can be calculated, along with the sound transmission loss.

Figures 5a and 5b plot the dispersion curves of the LRM plate with attached SDOF translational resonators for $\phi = 0°$ and $\phi = 90°$. Results show how a bandgap is created in the frequency region of negative effective mass density $f_z = 1589.5$ Hz $\leq f \leq f_z\sqrt{1+m_{\text{ratio}}} = 1741$ Hz, and how a good match between analytical and WFEM computations is obtained. The dispersion curves for $\phi = 0°$ of the LRM plate with attached SDOF rotational resonators is instead plotted in Figure 6a. Considering that the related undamped dynamic effective mass density can be written as $\rho_{\text{eff,ry,und}} = \rho + \frac{k_x^2 J_{\text{pua}}}{h(1-(\omega/\omega_{\text{ry}})^2)}$, the analytical dispersion curves

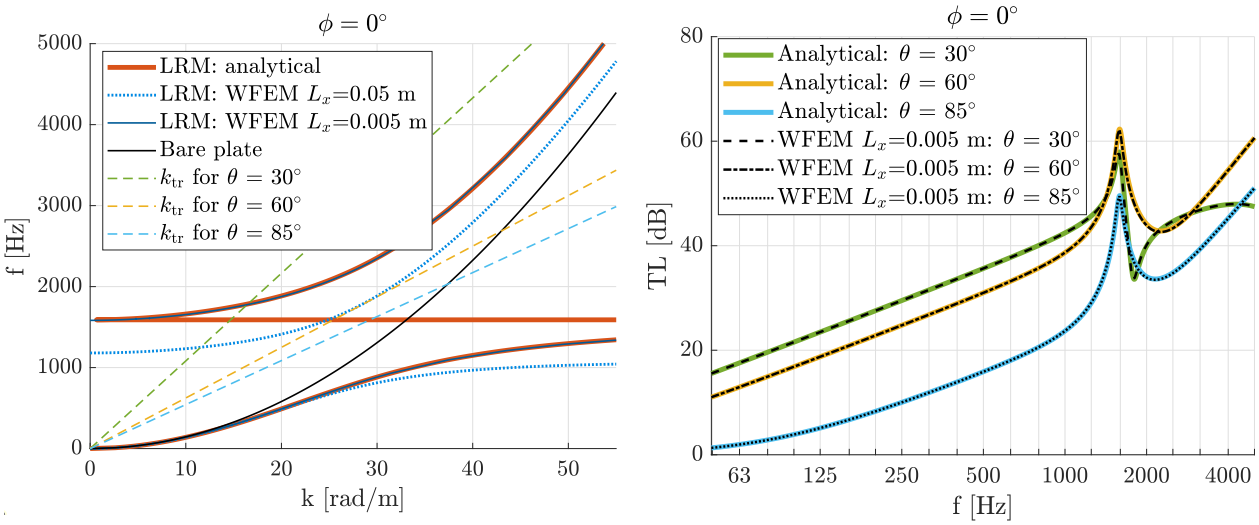


Figure 6: Dispersion relation (a) and sound Transmission Loss (b) for $\phi = 0°$ of the considered orthotropic LRM plate with periodically attached SDOF rotational resonators.

depend only on the inertia per unit of area of the resonators $J_{\text{pua}}$, and not on the specific UC dimensions. However, we see how the WFEM predictions and the agreement between the two models depend on the UC dimensions considered in the WFEM: the analytical model captures the behaviour of the system for relatively small UC (e.g. $L_{\text{x}} = 0.005$ m), while for larger UCs (e.g. $L_{\text{x}} = 0.05$ m) it exhibits still some differences with respect to the WFEM results, especially in terms of the frequency at which the discontinuity in the dispersion curve appears. Such discontinuity can be interpreted as an introduced zero-width bandgap: it has the same shape as for the bandgaps observed for LRMs with translational resonators (Figures 5a and 5b), but covers only a single frequency.

Figures 5c and 5d plot the TL curves for the LRM plate with SDOF translational resonators for $\phi = 0°, 90°$, while the TL predictions for the LRM plate with SDOF rotational resonators for $\phi = 0°$ and $L_{\text{x}} = 0.005$ m are shown in Figure 6b. Damping factors $\eta_0 = \eta_{\text{z}} = \eta_{\text{ry}} = 0.05$ are considered, and curves for different elevation angles $\theta$ are plotted. In general, we can see how a TL peak is introduced at the resonant frequency of the resonator. For coincidence frequencies $f_{\text{co}}(\phi, \theta)$ of the host structure above the created bandgap, e.g. for $\theta = 30°$, an additional low-frequency coincidence is introduced close to the upper bound of the bandgap [16]. The corresponding TL curve therefore exhibits a characteristic peak-dip shape close to the resonance-based bandgap, along with a second coincidence dip close to the one of the original bare plate. Instead, if the coincidence frequency $f_{\text{co}}(\phi, \theta)$ is sufficiently close to the (zero-width) bandgap, e.g. for almost grazing incidence $\theta = 85°$, no coincidence is achieved, neither close to the bandgap, nor close to the bare plate coincidence. In this case, the TL curve presents only a peak at the resonance frequency of the resonator, without any coincidence dip.

The coincidence suppression observed for almost grazing incidence is present also for diffuse field incidence [3, 4]: this is shown in Figures 7a and 7b, where a comparison is provided between the orthotropic LRM plates, the bare plate, and a bare plate with the same mass as the LRM plates. Results show how LRM treatments allow to achieve significant broadband TL improvements in orthotropic plates, and how the coincidence dip can be suppressed by a proper tuning of the bandgap frequency range.

## 4 Modelling and optimization of multimodal resonator layouts for orthotropic LRM plates

In this Section, the analytical model based on dynamic effective mass density will be used to analyze the behaviour of orthotropic LRM plates with complex multimodal resonator layouts. This follows the extrac-

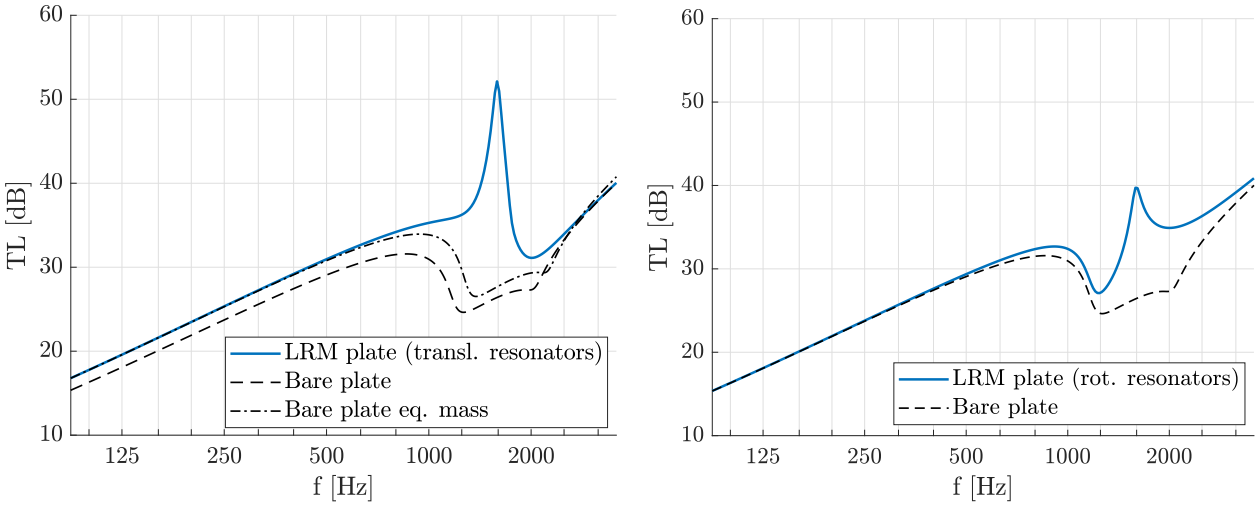


Figure 7: Diffuse field sound Transmission Loss of the considered orthotropic LRM plate, in the case of periodically attached (a) SDOF translational and (b) SDOF rotational resonators.

tion of translational and rotational modal effective masses from a simple modal analysis of the fixed-base resonator. The resulting computationally cheap analysis will be used for the efficient design optimization of the resonator layouts in order to maximize broadband sound insulation.

## 4.1 Considered multimodal resonator layouts and design variables

The present discussion will focus on the two multimodal resonator layouts shown in Figure 8, and attached to the previously introduced orthotropic plate. Resonators made by polymethyl methacrylate (PMMA) will be considered through the following material properties: $E = 4850$ MPa, $\nu = 0.31$, $\rho = 1200$ kg/m$^3$, $\eta = 0.05$.

Layout 1 consists of a bi-directional rotational resonator, where a mass is suspended by a vertical beam. In this case the two main modes of interest are related to rotations of the mass around the $x$ and $y$ axis, with corresponding bending of the vertical beam, and transfer of bending moments to the host structure influencing wave propagation along the $y$ and $x$ directions, respectively. Layout 2 is inspired by [2], and consists instead of a translational resonator with two resonating units, that are independently connected to the host structure and constituted by two separate cantilever beams with attached end-point masses. In this case the two main modes of interest will be related to the vertical motion of the masses, with transfer of vertical forces and bending moments to the host structure.

The layouts will be optimized to to maximize broadband sound insulation. This will be done by considering the design variables shown in Figure 8. In both cases, planar layouts extruded along $y$ with thickness $b$ are considered. For Layout 1, the design variables are related to the dimensions of the resonator base, of the vertical beam and of the end mass. For Layout 2, both resonant units share the same design variables related to the resonator base and the dimension $b$ in the $y$ direction, while the design variables related to the cantilever beams and the end masses are kept independent, in order to obtain different associated resonant frequencies.

## 4.2 Analysis methodology

The analytical model presented in Section 3, based on dynamic effective mass density, can be used to efficiently analyze the behaviour of LRM plates with complex multimodal resonator layouts. In this case, each mode can be associated with translational and rotational inertial contributions $m_z$, $J_{rx}$, $J_{ry}$, which can be extracted as modal effective masses from a simple modal analysis of the fixed-base resonator.

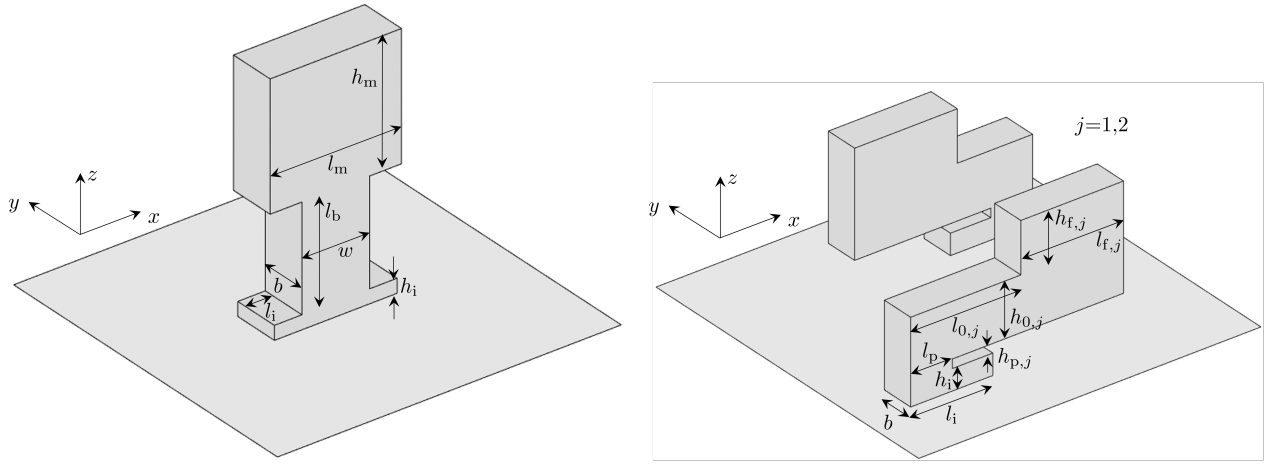


(a) (b)

Figure 8: Considered multimodal resonator layouts: (a) Layout 1, (b) Layout 2. The design variables used in the optimization process are also indicated.

After discretizing the resonator layout by linear hexaedral finite elements, the $k$-th eigenfrequency $\omega_{\mathrm{r},k}$ and the $k$-th mode shape $\boldsymbol{\phi}_{r,k}$ can be found by solving the following eigenvalue problem:

$$(-\omega_{\mathrm{r}}^2 \boldsymbol{M}_{\mathbf{r}} + \boldsymbol{K}_{\mathbf{r}})\boldsymbol{\phi}_{\mathbf{r}} = \mathbf{0} \tag{15}$$

where $\boldsymbol{M}_{\mathbf{r}}$ and $\boldsymbol{K}_{\mathbf{r}}$ are the assembled mass and stiffness matrices of the resonator for fixed-based boundary conditions. The eigenvalue problem in Eq. (15) is solved for a number $n_{\mathrm{m}}$ of modes such that all the modes below 3 times the maximum frequency of the analysis are included. Assuming mass normalized modes, the modal effective mass of mode $k$ along the kinematic direction $i$ = $z$, $\theta_{\mathrm{x}}$, $\theta_{\mathrm{y}}$ can be computed as [18]:

$$m_{i,k}^{\mathrm{eff}} = \Gamma_{i,k}^2, \qquad \Gamma_{i,k} = \boldsymbol{\phi}_{\boldsymbol{r},\boldsymbol{k}}^T \boldsymbol{M}_{\mathbf{r}} \boldsymbol{t}_{\boldsymbol{i}} \tag{16}$$

where $\Gamma_{i,k}$ is the modal participation factor corresponding to a unitary rigid body motion $\boldsymbol{t_i}$ imposed to the resonator along the $i$-th direction. Rigid rotations along $\theta_{\mathrm{x}}$ and $\theta_{\mathrm{y}}$ are imposed around a center of rotation positioned in correspondence of the center of the resonator base (or the resonating unit base), on the mid-plane of the host plate, i.e. at a distance $h$/2 from the resonator base.

The computed translational and rotational modal effective masses for each resonator mode can be summed to obtain the effective mass density of the multimodal LRM plate, that can be expressed as:

$$\rho_{\mathrm{eff}} = \rho \left( 1 + m_{\mathrm{ratio}} - \sum_{k=1}^{n_{\mathrm{m}}} \frac{m_{\mathrm{z},k}^{\mathrm{eff}}}{m_{\mathrm{UC}}} \right) + \sum_{k=1}^{n_{\mathrm{m}}} \frac{1}{h} \left( \frac{n k_{\mathrm{z},k}^{\mathrm{eff}} m_{\mathrm{z},k}^{\mathrm{eff}}}{k_{\mathrm{z},k}^{\mathrm{eff}} - m_{\mathrm{z},k}^{\mathrm{eff}} \omega^2} + \frac{n k_{\mathrm{y}}^2 k_{\theta_{\mathrm{x}},k}^{\mathrm{eff}} m_{\theta_{\mathrm{x}},k}^{\mathrm{eff}}}{k_{\theta_{\mathrm{x}},k}^{\mathrm{eff}} - m_{\theta_{\mathrm{x}},k}^{\mathrm{eff}} \omega^2} + \frac{n k_{\mathrm{x}}^2 k_{\theta_{\mathrm{y}},k}^{\mathrm{eff}} m_{\theta_{\mathrm{y}},k}^{\mathrm{eff}}}{k_{\theta_{\mathrm{y}},k}^{\mathrm{eff}} - m_{\theta_{\mathrm{y}},k}^{\mathrm{eff}} \omega^2} \right) \tag{17}$$

where the factor $\left( 1 + m_{\mathrm{ratio}} - \sum_{k=1}^{n_{\mathrm{m}}} \frac{m_{\mathrm{z},k}^{\mathrm{eff}}}{m_{\mathrm{UC}}} \right)$ is added to consider the quasi-static contribution of modes with higher order than the $n_{\mathrm{m}}$ considered ones, and the modal effective stiffnesses are found as $k_{i,k}^{\mathrm{eff}} = m_{i,k}^{\mathrm{eff}} \omega_{\mathrm{r},k}^2$. The computed effective mass density can be finally used in Eq. (3) and (4) to efficiently predict the TL of the orthotropic LRM plate when attaching the considered multimodal resonator layouts.

## 4.3 Optimized multimodal resonator layouts

The optimal resonator layouts are found by solving an optimization problem. As objective function, we maximize the single number rating $R_{\mathrm{A}}$ related to the standard ISO 717 [19]. $R_{\mathrm{A}}$ represents the A-weighted broadband sound insulation for pink noise excitation in the frequency range 100-3150 Hz, and can be found as $R_{\mathrm{A}} = R_{\mathrm{w}} + C$, with $R_{\mathrm{w}}$ and $C$ defined by the standard. A constraint is also imposed on the maximum

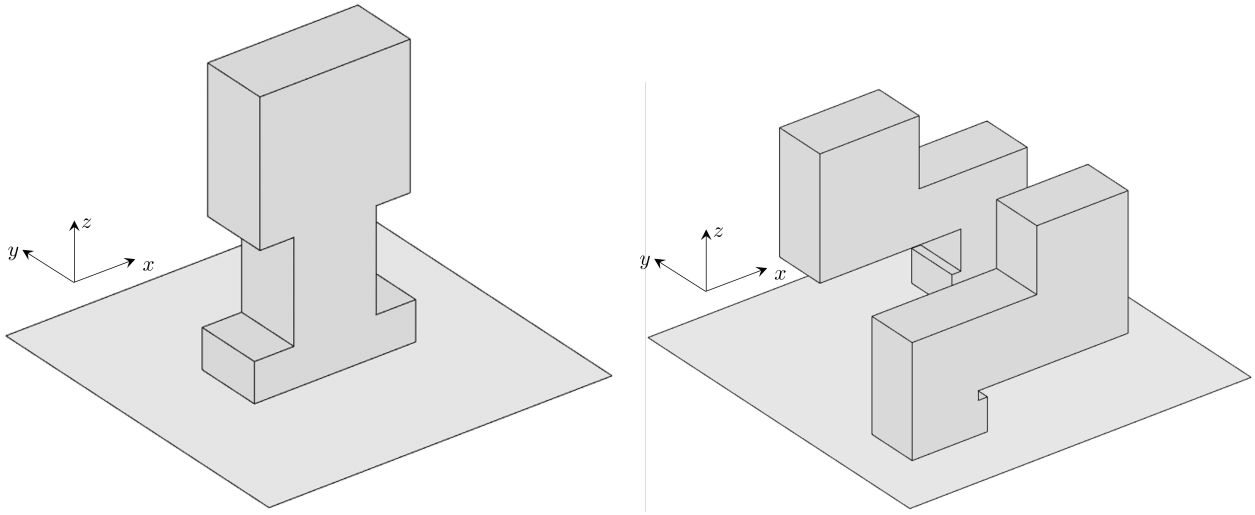


(a) (b)

Figure 9: Optimized resonator layouts: (a) Layout 1, (b) Layout 2.

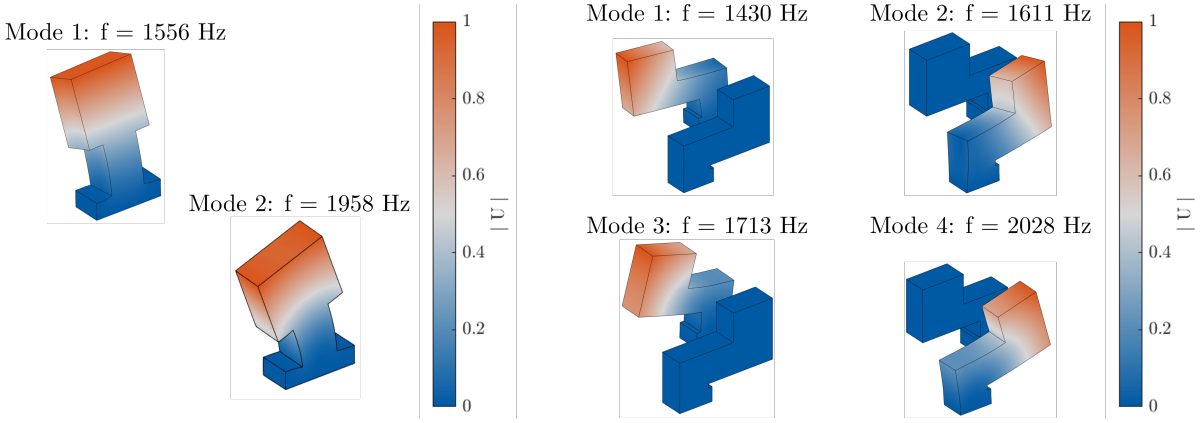


(a) (b)

Figure 10: Modes of interest for the optimized resonators: (a) Layout 1, (b) Layout 2.

resonator mass, that has to be lower then 20% of the bare plate mass. The considered optimization problem is therefore:

$$\begin{aligned} &\max && R_{\mathrm{A}} \\ &\text{subject to} && m_{\mathrm{ratio}} \leq 0.2 \end{aligned} \tag{18}$$

The optimization problem in Eq. (18) is solved using a Genetic Algorithm (GA) through the `ga` function from Matlab.

The optimized resonator layouts are shown in Figure 9, while the corresponding fixed-base modes of interest are shown in Figure 10, and the TL curves are represented in Figure 11. Also, Figure 11 compares the TL curves related to the LRM, to the original bare plate, and to bare plates with static masses equivalent to the LRMs, i.e. increased by 20%. We see how each mode of interest introduces a TL peak within the coincidence dip of the original bare plate. For Layout 1, the modes of interest are the two rotational ones around $x$ and $y$. Mode 1 corresponds to a rotation around the $x$ axis and is placed closer to the critical frequency observed along the stiffer direction $y$, while mode 2, corresponding to a rotation around $y$, is placed closer to the critical frequency observed along $x$. For Layout 2 the main peaks are related to the two translational modes (modes 3 and 4), but also smaller peaks related to rotational modes (modes 1 and 2) are exploited by the optimizer. These modes correspond to translations of the suspended masses along $y$, and transfer bending moments around $x$ through the small distance of the masses from the host structure along $z$. Modes 1 and

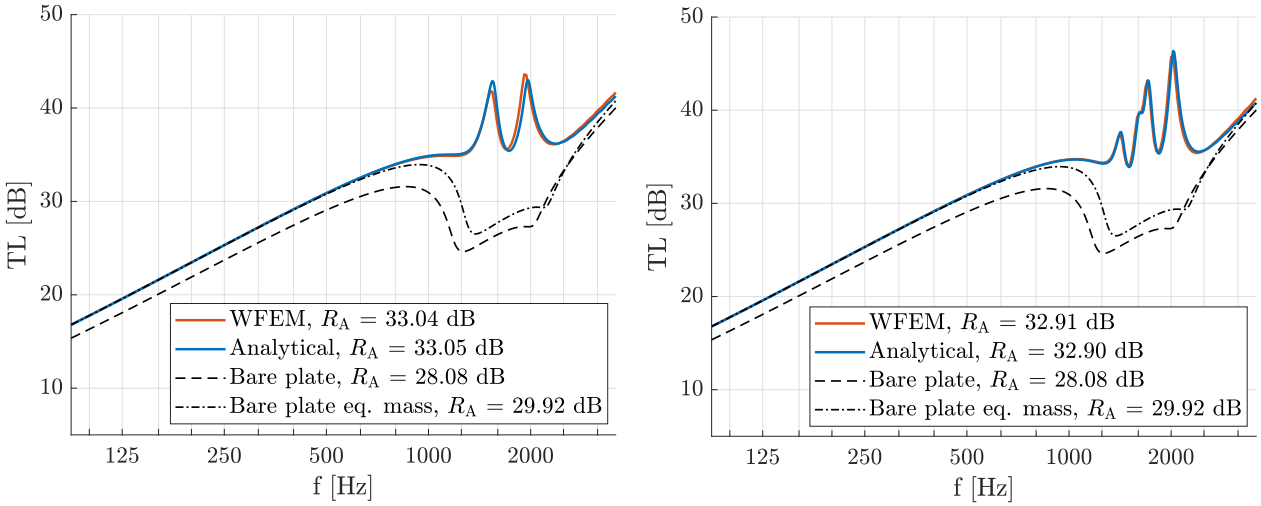


Figure 11: Transmission Loss curves of the orthotropic LRM plate with attached optimized resonators: (a) Layout 1, (b) Layout 2.

Table 1: Comparison between the analytical model and the WFEM in terms of computational cost. Diffuse field TL computations of the orthotropic LRM plate are considered, when attaching Layout 1 of the resonator.

| Method | Num. freq. | Dim. grid $(\phi, \theta)$ | Comp. time |
|---|---|---|---|
| Analytical | 257 | 61×31 | 0.21 s |
| WFEM | 257 | 61×31 | 15 h 45 min (single core)<br>3 h 48 min (parallelized on 6 cores) |

2 therefore mainly influence wave propagation along $y$. For both Layout 1 and Layout 2, we can see how the original coincidence dip is suppressed by the introduced resonant TL peaks. This leads to an eventual improvement of $R_A$ by ≈4 dB with respect to bare plates with equivalent mass.

In order to validate the employed analysis methodology and the optimized layouts, a comparison is performed between analytical and WFEM TL predictions. In the UC model used in the WFEM, the host plate is discretized by linear Kirchhoff plate finite elements, while the attached resonator is discretized by linear hexaedral finite elements. In the resonator discretization, the same mesh is considered both for the WFEM and for the fixed-base modal analysis in the analytical model. The comparison between the two methods also focuses on computational costs, reported in Table 1 for TL curves computed for the same 257 frequencies, using the same grid to numerically integrate $\tau(\phi, \theta)$ in Eq. (5), and considering an Intel(R) Core(TM) i7-9850H CPU (2.60GHz). The reported computational costs are related to Layout 1, when both methods are fully implemented in Matlab, including the finite element formulation and computations. Results show how the computational cost associated with the analytical model is extremely low with respect to the WFEM, while no significant degradation of the results is observed: the TL curves overlap very well, and very close $R_A$ values are obtained.

## 5 Conclusions

In this paper, the potential of employing rotational and multimodal resonators in orthotropic locally resonant metamaterials (LRM) plate has been investigated.

An analytical vibroacoustic description of orthotropic LRM plates with periodically attached SDOF translational and SDOF rotational resonators has been derived, focusing on the related dynamic effective mass

density. The developed analytical model has been extended to consider complex multimodal resonator layouts, with both translational and rotational modes of interest. This is done by defining the effective mass density as function of the modal effective masses extracted from a simple modal analysis of the fixed-base resonator. The accuracy of the proposed analytical models has been verified through comparisons with Wave and Finite Element Method (WFEM) predictions, with respect to which an extreme reduction of the computational costs has been obtained.

The proposed efficient prediction model has been used in combination with numerical optimization to automatically design the geometrical layout of two multimodal resonators, exploiting respectively mainly rotational and translational modes. The layouts have been optimized to maximize broadband sound insulation through the single number rating $R_{\mathrm{A}}$, achieving significant broadband TL improvements and suppressing the broad coincidence dip of the original bare orthotropic plate.

The demonstrated potential of employing multimodal resonators in LRMs can be further extended by widening the design space of the considered structural optimization methods. For example, shape optimization and topology optimization can explore different structural shapes and go beyond usual design concepts, fostering innovation towards new multimodal resonator layouts.

## Acknowledgements

The presented work has been carried out within the ERC Starting Grant 714591 VirBAcous. The authors gratefully acknowledge the financial support of the European Research Council (ERC).

## References

[1] C. Claeys, K. Vergote, P. Sas, and W. Desmet, "On the potential of tuned resonators to obtain low-frequency vibrational stop bands in periodic panels," *Journal of Sound and Vibration*, vol. 332, no. 6, pp. 1418–1436, 2013.

[2] L. Van Belle, C. Claeys, E. Deckers, and W. Desmet, "The impact of damping on the sound transmission loss of locally resonant metamaterial plates," *Journal of Sound and Vibration*, vol. 461, p. 114909, 2019.

[3] J. Vazquez Torre, J. Brunskog, and V. Cutanda Henriquez, "An analytical model for broadband sound transmission loss of a finite single leaf wall using a metamaterial," *Journal of the Acoustical Society of America*, vol. 147, no. 3, pp. 1697–1708, 2020.

[4] J. Vazquez Torre, J. Brunskog, V. Cutanda Henriquez, and J. Jung, "Hybrid analytical-numerical optimization design methodology of acoustic metamaterials for sound insulation," *Journal of the Acoustical Society of America*, vol. 149, no. 6, pp. 4398–4409, 2021.

[5] N. Rocha de Melo Filho, C. Claeys, E. Deckers, and W. Desmet, "Optimised thermoformed metamaterial panel design with a foam core for improved noise insulation performance," in *Proceedings of ISMA 2020*, Desmet, W. KU Leuven, 2020, pp. 2513–2524.

[6] D. Giannini, G. Bonaccorsi, and F. Braghin, "Size optimization of MEMS gyroscopes using substructuring," *European Journal of Mechanics - A/Solids*, vol. 84, p. 104045, 2020.

[7] D. Giannini, N. Aage, and F. Braghin, "Topology optimization of MEMS resonators with target eigenfrequencies and modes," *European Journal of Mechanics - A/Solids*, vol. 91, p. 104352, 2022.

[8] D. Giannini, M. Schevenels, and E. Reynders, "Topology optimization of plate structures for sound transmission loss improvement in specific frequency bands," in *Proceedings of the 12th European Congress and Exposition on Noise Control Engineering, Euronoise 2021*. sociedade Portuguesa de Acustica, 2021, pp. 1435–1442.

[9] T. Wang, M. Sheng, Z. Guo, and Q. Qin, "Acoustic characteristics of damped metamaterial plate with parallel attached resonators," *Archives of Mechanics*, vol. 69, pp. 29–52, 01 2017.

[10] B. Mace and E. Manconi, "Modelling wave propagation in two-dimensional structures using finite element analysis," *Journal of Sound and Vibration*, vol. 318, no. 4–5, pp. 884–902, 2008.

[11] B. Assouar, M. Oudich, and X. Zhou, "Acoustic metamaterials for sound mitigation," *Comptes-Rendus Physique*, vol. 17, no. 5, pp. 524–532, 2016, phononic crystals / Cristaux phononiques.

[12] E. Deckers, S. Jonckheere, L. Van Belle, C. Claeys, and W. Desmet, "Prediction of transmission, reflection and absorption coefficients of periodic structures using a hybrid wave based - finite element unit cell method," *Journal of Computational Physics*, vol. 356, pp. 282–302, 2018.

[13] L. Van Belle, N. Rocha de Melo Filho, M. Clasing, C. Claeys, E. Deckers, F. Naets, and W. Desmet, "Fast metamaterial design optimization using reduced order unit cell modeling," in *Proceedings of ISMA 2020*, 10 2020.

[14] F. Fahy and P. Gardonio, *Sound and structural vibration: radiation, transmission and response*, 2nd ed. Oxford, UK: Academic Press, 2007.

[15] J. Rindel, *Sound insulation in buildings*. Boca Raton, FL: CRC Press, 2018.

[16] C. Claeys, P. Sas, and W. Desmet, "On the acoustic radiation efficiency of local resonance based stop band materials," *Journal of Sound and Vibration*, vol. 333, no. 14, pp. 3203–3213, 2014.

[17] Y. Yang, B. Mace, and M. Kingan, "Vibroacoustic analysis of periodic structures using a wave and finite element method," *Journal of Sound and Vibration*, vol. 457, pp. 333–353, 2019.

[18] J. Wijker, *Modal Effective Mass*. Berlin, Heidelberg: Springer Berlin Heidelberg, 2008, pp. 247–263.

[19] *ISO 717-1: Acoustics – Rating of sound insulation in buildings and of building elements – Part 1: Airborne sound insulation*, International Organization for Standardization, 2013.